Chromium phosphide CrP as highly active and stable electrocatalysts for oxygen electroreduction

Junfeng Liu,[a] Xiaoting Yu,[a] Ruifeng Du,[a] Chaoqi Zhang,[a] Ting Zhang,[b] Jordi Llorca,[c] Jordi Arbiol,[b,d] Ying Wang,[e,*] Michaela Meyns,[a,#,*] Andreu Cabot[a,d,*]

[a] Catalonia Institute for Energy Research (IREC), Sant Adrià de Besòs, 08930 Barcelona, Spain

[b] Catalan Institute of Nanoscience and Nanotechnology (ICN2), CSIC and BIST, Campus UAB, Bellaterra, 08193 Barcelona, Catalonia, Spain

[c] Institute of Energy Technologies, Department of Chemical Engineering and Barcelona Research Center in Multiscale Science and Engineering, Universitat Politecnica de Catalunya, Eduard Maristany 10-14, 08019 Barcelona, Spain

[d] ICREA, Pg. Lluis Companys 23, 08010 Barcelona, Catalonia, Spain

[e] State Key Laboratory of Rare Earth Resource Utilization, Changchun Institute of Applied Chemistry, Chinese Academy of Sciences, Changchun 130022, P. R. China

[#] Current address: Alfred-Wegener-Institute, Helmholtz Centre for Polar and Marine Research, Biologische Anstalt Helgoland, Kurpromenade 201, 27498 Helgoland, Germany

* Corresponding Author

Y. Wang: ywang_2012@ciac.ac.cn

M. Meyns: michaela.meyns@awi.de

A. Cabot: acabot@irec.cat

ABSTRACT

Catalysts for oxygen reduction reaction (ORR) are key components in emerging energy technologies such as fuel cells and metal-air batteries. Developing low-cost, high performance and stable electrocatalysts is critical for the extensive implementation of these technologies. Herein, we present a procedure to prepare colloidal chromium phosphide CrP nanocrystals and we test their performance as ORR electrocatalyst. CrP-based catalysts exhibited remarkable activities with a limiting current density of 4.94 mA cm^{-2} at 0.2 V, a half-potential of 0.65 V and an onset potential of 0.8 V at 1600 rpm, which are comparable to commercial Pt/C. Advantageously, CrP-based catalysts displayed much higher stabilities and higher tolerances to methanol in alkaline solution. Using density functional theory calculations, we demonstrate CrP to provide a very strong chemisorption of O_2 that facilitates its reduction and explains the excellent ORR performance experimentally demonstrated.

Keywords: metal phosphide; colloidal synthesis; electrocatalysis; oxygen reduction

1. Introduction

The oxygen reduction reaction (ORR) is an essential process in particularly appealing energy conversion and storage technologies, such as fuel cells and metal air batteries. These technologies rely on an oxygen cathode where ambient oxygen is reduced. The complete ORR requires the participation of 4 electrons, making it very sluggish and limiting the overall performance of these devices. To accelerate this reaction, Pt or Pt-based alloys are generally required,[1,2] what strongly increases the device cost and constitutes one of the major barriers toward commercialization. Hence, considerable efforts are involved in the design and production of ORR catalysts that are free of Pt and Pt-group metals. ORR catalysts have been searched within most material families, including metal oxides,[3] carbides,[4] phosphides,[5-10] chalcogenides[11] and even metal-free catalysts.[12,13] Among them, phosphides are particularly interesting due to their suitable stability, excellent electrical conductivities and the high abundance and low cost of phosphorous. Within this family, Co_2P,[7] CoP,[8] PdP_2[9] and

Ru_2P[10] have already demonstrated excellent ORR activities, but stability and/or reliance on expensive noble metals is still an issue.

In spite of its suitable characteristics, chromium phosphide has been surprisingly ignored not only as ORR catalysts but also for its other potential technological applications. This is particularly noteworthy taking into account the high abundance of chromium in the earth crust, above that of nickel, zinc or copper to cite some examples. Besides, chromium global annual production is very high due to its use in metallurgy, what translated in low costs. Chromium phosphide is a hard-wearing metallic conductor that displays high thermal stability, good resistivity to oxidation and anti-corrosion toward water and diluted acids.[14-18] These properties make CrP an appealing candidate in a wide range of applications. However, very few papers have reported the synthesis and applications of chromium phosphides.[14-16] In particular, CrP has been produced in film form by chemical vapour deposition,[14-16] but never in the form of nanoparticles.

In a previous work, we showed that triphenyl phosphite (TPP) can be used as a low-cost and air-stable phosphorous precursor to produce several binary and ternary metal phosphides such as Ni_2P, Co_2P, Fe_2P, Cu_3P, MoP and $Ni_{2-x}Co_xP$.[19,20] However, due to the low-boiling point of the reaction mixture in our previously reported procedure, attempts to produce metal phosphides that required higher crystallization temperatures were not successful. In the present work, we demonstrate the production of CrP nanocrystals (NCs) using TPP as a highly suitable phosphorous precursor and a high boiling point solvent. The produced CrP NCs were combined with carbon and tested as electrocatalyst for ORR. Our preliminary assessment of the activity of CrP NCs demonstrates CrP-based catalysts to be highly suitable for oxygen electroreduction.

2. Experimental

2.1. Chemicals

Triphenyl phosphite (TPP, 99%) was purchased from Alfa Aesar. Chromium hexacarbonyl ($Cr(CO)_6$, 99+%) and oleylamine (OAm, approximate C18 content 80-90%) were purchased from ACROS Organics. Carbon-supported Pt NCs (Pt/C, 20 wt% Pt), Nafion (5 wt% in a

mixture of low aliphatic alcohols and water) and potassium hydroxide (KOH, 85%) were purchased from Sigma Aldrich. Chloroform, acetone and ethanol were of analytical grade and obtained from various sources. Milli-Q water was supplied by a Purelab flex from Elga. All chemicals were used as received without further purification.

2.2. Synthesis of CrP NCs

All reactions were carried out under argon atmosphere using standard Schlenk line techniques. In a typical synthesis, 10 mL of OAm and 1 mL of TPP were mixed in a 50 mL three-neck flask equipped with a condenser and a stir bar. The system was heated to 120 °C under Ar flow and maintained at this temperature for at least 1 h. Then, 110 mg (0.5 mmol) of $Cr(CO)_6$ was quickly added into the flask under Ar flow. The mixture was heated to 320 °C in 20 min and kept at that temperature for 2 h. Afterward, the flask was allowed to cool down to room temperature by removing the heating mantle. Excess ethanol was added to the black product followed by centrifugation at 5000 rpm (3200 g) for 5 min. Purification was achieved by another two dispersion/precipitation steps using chloroform/ethanol with a 1:3 volume ratio. Finally, the supernatant was discarded and the precipitated material was collected and dried in ambient conditions.

2.3. Material characterization

Transmission electron microscopy (TEM) characterization was carried out using a ZEISS LIBRA 120, operating at 120 kV and a JEOL 1011 operating at 100 kV. Carbon-coated TEM grids from Ted-Pella were used as substrates. Powder x-ray diffraction (XRD) patterns were collected from NCs supported on a Si (501) substrate using a Bruker-AXS D8 Advanced x-ray diffractometer with Ni-filtered (2 μm thickness) Cu K radiation (λ = 1.5406 Å) operating at 40 kV and 40 mA. A LynxEye linear position-sensitive detector was used in reflection geometry. High-resolution TEM (HRTEM) studies were conducted using a field emission gun FEI Tecnai F20 microscope at 200 kV with a point-to-point resolution of 0.19 nm. High angle annular dark-field (HAADF) STEM was combined with electron energy loss spectroscopy (EELS) in the Tecnai F20, by using a GATAN QUANTUM filter. Scanning electron microscopy (SEM) analyses were carried out using a ZEISS Auriga microscope with an energy dispersive x-ray

spectroscopy (EDS) detector operating at 20 kV. Dispersive spectrometer Jobin-Yvon Lab Ram HR 800 with Olympus BXFM microscope optic was used to obtain Raman spectra. X-ray photoelectron spectroscopy (XPS) was carried out on a SPECS system equipped with an Al anode XR50 source operating at 150 W and a Phoibos 150 MCD-9 detector. The pressure in the analysis chamber was below 10^{-7} Pa. The area analyzed was about 2 mm × 2 mm. The pass energy of the hemispherical analyzer was set at 25 eV and the energy step was set at 0.1 eV. Data processing was performed with the CasaXPS program (Casa Software Ltd., UK). Binding energy values were corrected using the C 1s peak at 284.8 eV. Fourier transform infrared spectroscopy (FTIR) was performed on an Alpha Bruker FTIR spectrometer with a platinum attenuated total reflectance (ATR) single reflection module.

2.4. Electrochemical measurements

The as-synthesized CrP NCs were mixed with carbon black (Vulcan XC-72) with a weight ratio of 30% in a mixture chloroform and ethanol (1:1). The CrP and carbon mixture was sonicated for 1 h and then washed several times with chloroform and acetone. The precipitate was dried in air and then annealed at 450 °C under 5% H_2/Ar for 2 h to remove surface ligand. The catalysts ink were prepared by mixing 5 mg of the annealed CrP/C composite, 1 mL of 1:1 (v:v) deionized water/isopropanol and 17.5 μL of 5 wt% of Nafion to form a homogenous ink by sonicating for 1 h. Subsequently, 5 μL of the suspension was deposited onto a cleaned glassy carbon (GC, 3 mm in diameter) rotating disk electrode (RDE) with a geometric area of 0.07 cm^2, and dried in ambient conditions before electrochemical measurements. For comparison, electrodes based on commercial Pt/C (20 wt% Pt) catalyst were also fabricated following the above process.

Electrochemical measurements were conducted at room temperature on a BioLogic Electrochemical workstation using a standard three-electrode cell with the fabricated GC electrode as working electrode, Pt mesh as counter electrode and Hg/HgO as reference electrode. The linear sweep voltammetry (LSV) curves for ORR measurements were conducted from 0.2 to -0.7 V versus Hg/HgO at a scan rate of 5 mV s^{-1} with different rotating rates in O_2-saturated 0.1 M KOH electrolyte. The cyclic voltammetry (CV) measurements were performed at a scan rate of 5 mV s^{-1} without rotating in O_2 or Ar-saturated 0.1 M KOH electrolyte. To evaluate the

catalyst durability, chronoamperometry was collected at -0.3 V versus Hg/HgO in O_2-saturated electrolyte with a rotating rates of 200 rpm. Methanol tolerance measurements were conducted under the same condition as chronoamperometric tests but added 3M methanol at 1000 s and for comparison, another same amount of H_2O was added at 2000 s. As a reference electrode, Hg/HgO calibrated with respect to the reversible hydrogen electrode (RHE) in all measurements (+0.866 V vs RHE) was used.

2.5. Density functional theory (DFT)

The electronic structure and energy calculations were carried out by spin-polarized DFT using the Vienna ab initio simulation package (VASP).[21-24] The projector augmented wave (PAW) potentials were used to describe ion cores and valence electrons interactions.[25,26] The adopted exchange-correlation potential was the Perdew-Burke-Ernzerhof generalized gradient approximation (PBE GGA).[27] A kinetic energy cut off of 350 eV was used with a plane-wave basis set. The integration of the Brillouin zone was conducted using a 1×1×1 Monkhorst-Pack grid.[28] The last two layers were fixed and all the other atoms were fully relaxed until the force was converged to 0.05 eV/Å and the total energy was converged to 1.0×10^{-4} eV/atom.

A (211) surface was cut based on the bulk structure of CrP and a model with 1×2 unit cell and 6 layers was established. To avoid image interactions, a sufficiently large vacuum of 10.0 Å was taken along the z-axis.

The adsorption energy (E_{ads}) of nitrobenzene was defined as follows:

$$E_{ads} = E_{substrate+adsorbates} - E_{adsorbates} - E_{substrate} \quad (1)$$

where $E_{substrate+adsorbates}$, $E_{adsorbates}$, and $E_{substrate}$ are the total energies of adsorbate molecules and the CrP substrate, a gas phase adsorbate, and an isolated substrate, respectively. A negative value indicates an exothermic chemisorption.

The free energy diagrams of the oxygen reduction reactions were evaluated by the method of Nørskov et al.[29] Free energy change from initial states to final states of the reaction was calculated according to the following equation:

$$\Delta G = \Delta E + \Delta ZPE - T\Delta S + \Delta G_U + \Delta G_{pH} + \Delta G_{field} \qquad (2)$$

where $\boldsymbol{\Delta E}$ is the energy difference between reactants and products, obtained from DFT calculations; $\boldsymbol{\Delta ZPE}$ and $\boldsymbol{\Delta S}$ are the energy differences in zero-point energy and entropy; T is temperature considered to be 298.15 K; $\Delta G_U = eU$, where U is the electrode potential with respect to standard hydrogen electrode and e is transferred charge; ΔG_{pH} is defined as $k_B Tln10 \times pH$, where k_B is the Boltzmann constant. In this study pH=13 was chosen for alkaline medium according to experimental condition (0.1 M KOH solution). ΔG_{field} is the free energy correction resulting from the electrochemical double layer, which was neglected in the present study according to the previous studies.[29] The free energy of H_2O was calculated in the gas phase with a pressure of 0.035 bar, which is the equilibrium vapor pressure of H_2O at 298.15 K. The free energy of O_2 is obtained from the free energy change of the reaction $O_2 + 2H_2 \rightarrow 2H_2O$, which is -4.92 eV at 298.15 K and a pressure of 0.035 bar. According to a computational hydrogen electrode model suggested by Nørskov et al.,[29] the free energy of $(H^+ + e^-)$ in solution at standard conditions is assumed as the energy of 1/2 H_2. The free energy of OH^- was derived from the reaction $H^+ + OH^- \rightarrow H_2O$, which was in equilibrium in water solution.[30] The entropies and vibrational frequencies of O_2, H_2, and H_2O in gas phase were taken from the NIST database. Zero-point energy and entropies of the adsorbed species were estimated from the vibrational frequencies.

3. Results and discussion

CrP NCs were produced from the reaction of chromium hexacarbonyl and TPP in oleylamine (OAm), as detailed in the experimental section. **Figure 1a** shows a representative TEM micrograph of the NCs produced following this procedure. NCs showed spheroidal geometry with an average size of 17 ± 3 nm (**Figure 1b**). XRD patterns showed the NCs to have the CrP orthorhombic phase, with pnma space group

(**Figure 1f**). HRTEM analysis confirmed their orthorhombic phase with a= 5.3600 Å, b= 3.1140 Å and c= 6.0180 Å (**Figure 1c-e**). HAADF-STEM and STEM-EELS elemental composition maps revealed all NCs to contain Cr and P and to have both elements uniformly distributed throughout each NC (**Figure 1g**). No secondary phases were detected by XRD, HRTEM and STEM-EELS analyses. Extensive SEM-EDX analysis showed the as-synthesized CrP NCs to have an excess of phosphorous, P/Cr = 1.4 (**Figure S1**, supporting information), which could be attributed to the presence of TPP or an oxidized form of the phosphorous precursor as ligand on the NCs surface.

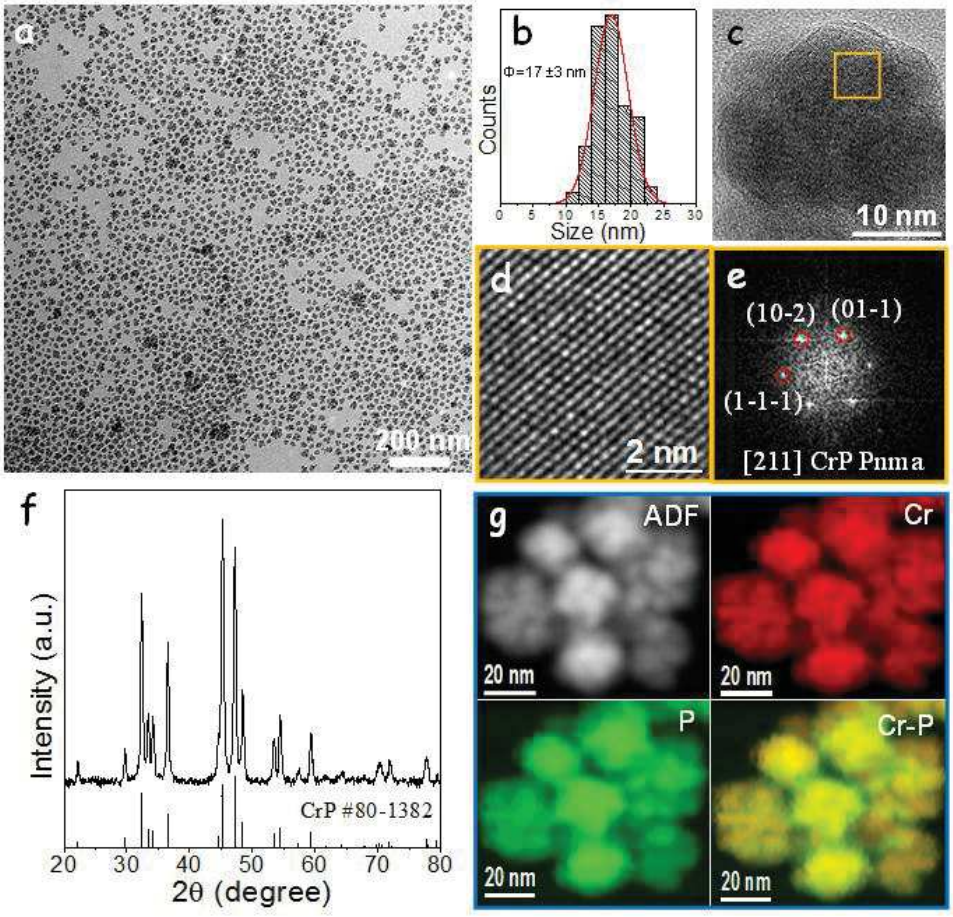

Figure 1. (a) Representative TEM micrograph of CrP NCs. (b) Histogram for the measured particle size distribution centered at 17 ± 3 nm. (c) HRTEM image of a single CrP NC. (d) Detail of the squared regions of the single CrP NC. (e) Its respective power spectrum fitting with the CrP orthorhombic phase. (f) XRD pattern of CrP NCs including the JCPDS #80-1382 reference. (g) HAADF-STEM micrograph of some CrP NCs and areal density of each of the elements extracted from the EELS spectrum image.

Figure 2 shows the Cr 2p, P 2p and valence band region of the XPS spectra of CrP NCs. The Cr 2p region showed Cr to be present at the NC surface in at least three chemical environments. Approximately 30% of the detected Cr was found in a chemical state compatible with CrP (P $2p_{3/2}$ = 575.0 eV). The other two chemical environments, a Cr^{3+} (P $2p_{3/2}$ = 578.0 eV) and a Cr^{n+} (Cr $2p_{3/2}$ = 579.8 eV), were associated with a slight surface oxidation of the NCs to Cr(III) phosphate, Cr_2O_3, CrO_3 and/or $CrO_2(OH)_2$ environments.[31,32] The oxidation of the outermost CrP surface probably resulted from the exposure of the sample to air before XPS measurement.

At least two P chemical states could be identified from XPS analysis of the P 2p electron states. A P $2p_{3/2}$ peak at 130.0 eV matched well with P in a metal phosphide environment such as CrP. This component accounted for 39% of the P in the outermost 2-3 nm surface of the NCs. The second component, accounting for 61% of the P detected, was found at a higher binding energy, P $2p_{3/2}$ = 134.1 eV, which we assigned to a chromium phosphate chemical environment resulting from the NC surface oxidation and/or a phosphite derived from the presence of phosphorous ligand on the NC surface. The atomic ratio of P and Cr at the NC surface detected by XPS was P/Cr = 2.65, suggesting a highly P-rich NC surface, which was consistent with the overall excess of P on the NCs detected by EDX measurement and further pointed out to a surface localization of the additional P. As shown in **Figure 2c**, a significant density of occupied states could be detected by XPS at the material Fermi level, which probed the metallic or highly degenerated character of the produced CrP.

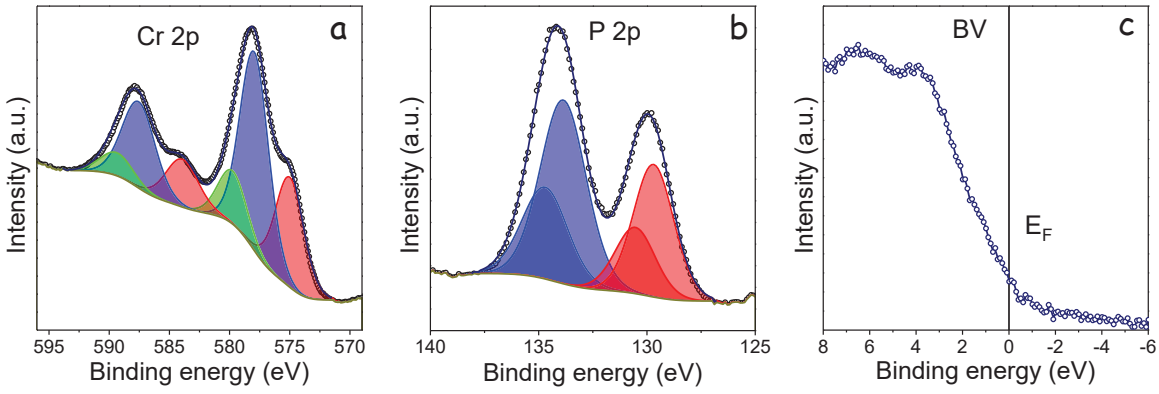

Figure 2. (a) Representative Cr 2p (a), P 2p (b) and valence band (c) regions of the XPS spectrum of CrP NCs.

The presence of OAm and phosphorous ligand on the NC surface was confirmed by FTIR analysis. As shown in **Figure 3**, the FTIR spectrum of the as-produced CrP NCs displayed peaks at 2906 and 2839 cm^{-1} attributed to the C-H stretching vibration of the alkyl group of OAm. Additionally, peaks attributed to the bending vibration of N-H at 1594 cm^{-1} and C-H at 1439 cm^{-1} were also identified. These features were slightly shifted compared with pure OAm, consistently with its binding to the NCs surface. A peak at 3130 cm^{-1} was assigned to the stretching vibration of =CH from the TPP phenyl group, which also appeared shifted with respect to pure TPP (3055 cm^{-1}). The FTIR spectrum of TPP displays several additional peaks between 600 to 1200 cm^{-1}. The peak at 1181 cm^{-1} is attributed to the stretching vibration of C-O and the peaks at 854 and 681 cm^{-1} were assigned to the bending vibration of C-H of the phenyl group. However, those peaks merged into a broad band centered at 870 cm^{-1} in the FTIR spectra of as-produced CrP NCs. The absence of all these features in the FTIR spectra of the final NCs after annealing under H_2/Ar atmosphere confirmed the elimination of organic ligands from the NC surface.

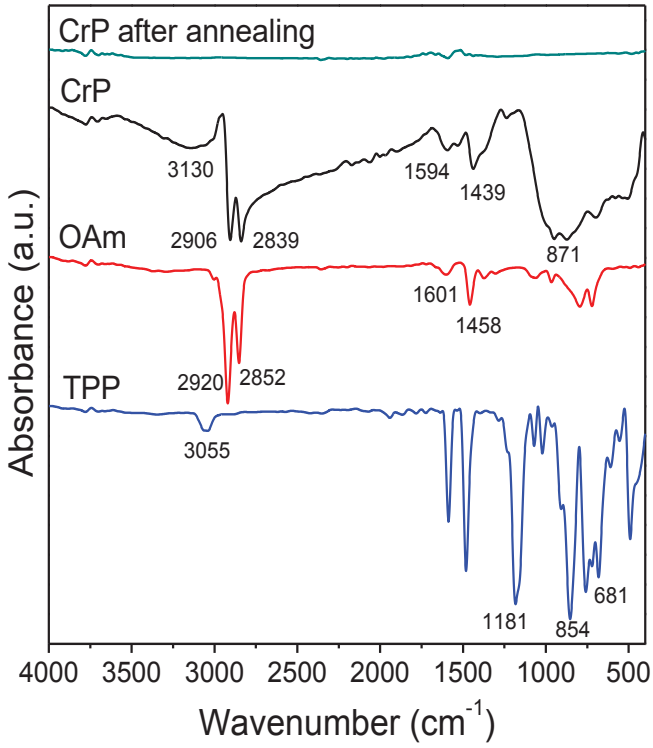

Figure 3. FTIR of OAm, TPP, as-produced CrP NCs and CrP after annealing at 450 °C for 2 h under H_2/Ar.

The electrocatalytic performance toward ORR of CrP NCs was evaluated in alkaline media. To prepare the CrP catalyst, CrP NCs were supported on carbon black to a weight ratio 3:7 (CrP NCs/C) through sonication and subsequent annealing at 450 °C under H_2/Ar. The catalyst was measured using a three-electrode system in O_2-saturated 0.1 M KOH (see experimental section for details). CVs were initially measured both in Ar and in O_2 saturated electrolyte, as shown in **Figure 4a**. Beyond the non-Faradic current characteristic of a double-layer charge-discharge, no noticeable features were observed for CrP catalyst within an Ar-saturated electrolyte. On the other hand, when the electrolyte was saturated with O_2, a cathodic peak centered at 0.63 V was clearly detected, indicating remarkable electrocatalytic activity toward ORR. **Figure 4b** shows polarization curves measured at different electrode rotation speeds, from 400 to 2500 rpm. As expected, the limiting current density increased with the rotation speed due to the promoted diffusion of oxygen around the electrode surface. The limiting current density of CrP-based electrodes at 0.2 V under 1600 rpm reached 4.94 mA cm^{-2}, with a half-potential of 0.65 V and an onset potential of 0.8 V. These values were comparable to those obtained with a commercial Pt/C electocatalyst, which provided a limiting current density of 5.63 mA cm^{-2} with a half-potential of 0.79 V and an onset potential of 0.95 V (**Figure 4d**).

The excellent ORR activity of the CrP electrocatalysts was further confirmed by small Tafel slopes, 64 mV dec^{-1}, indicating highly favorable reaction kinetics that translated into a high sensitivity of the electrocatalyst activity to the applied potential (inset in **Figure 4d**). Notice that, in the present work, CrP NCs were supported on low-cost commercial carbon, thus the measured catalytic performance did not rely on the electrocatalytic activity of doped graphenes,[33] carbon nanotubes[34] or highly ordered porous carbon matrices.[35] It is reasonable to assume that the use of high conductivity and active carbon supports could further improve performance, although at expenses of an extra cost.

The ORR kinetics of the CrP electrode was further analyzed by the Koutecky-Levich plots calculated from the measured LSV curves. As shown in **Figure 4c**, the Koutecky-Levich plots exhibited good linearity and approximately parallel dependences of the inverse of the current density with the square root of the rotation speed for applied voltages in the range from 0.2 to 0.6 V. This indicated first-order reaction kinetics with the oxygen concentration and denoted that,

within the studied range, electron transfer numbers for ORR did not depend on the applied potential.[36,37] The calculated electron transfer number for CrP electrocatalysts toward ORR was from 3.8 to 4.1, showing a high selectivity toward total oxygen reduction and the dominance of the one-step 4-electron oxygen reduction pathway.

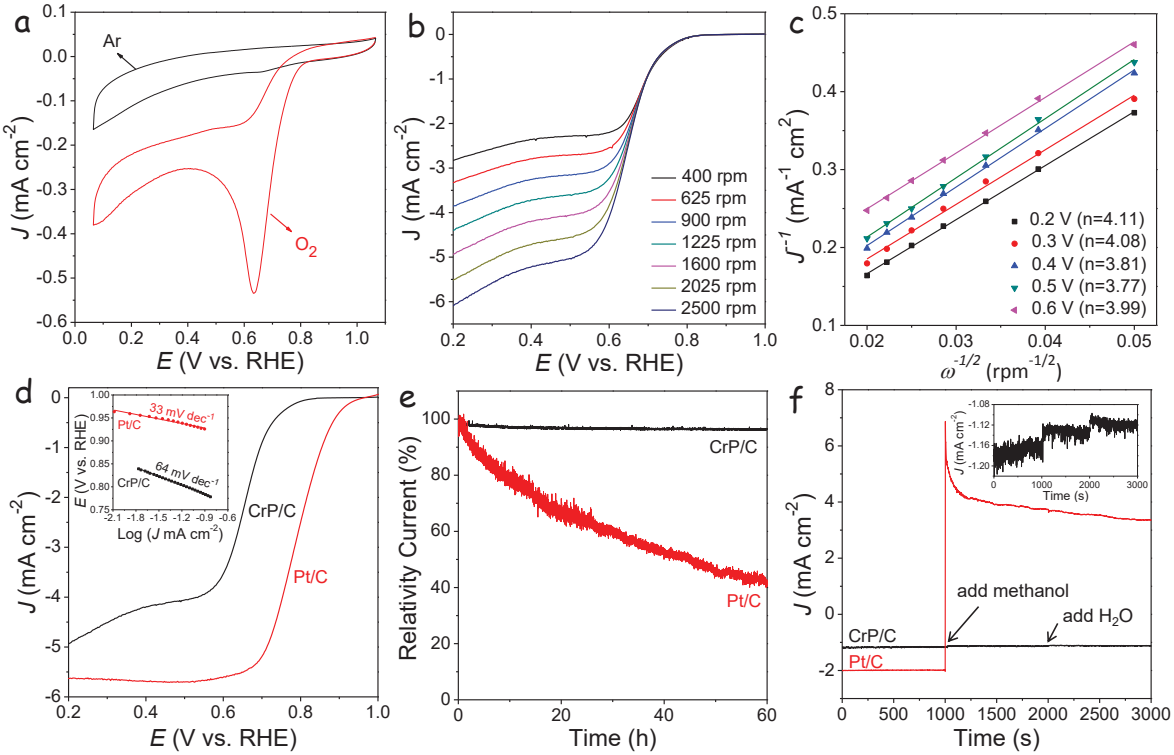

Figure 4. (a) CV curves of CrP/C in Ar- and O_2-saturated 0.1 M KOH solutions. (b) LSV curves of CrP/C at various rotating rates in O_2-saturated 0.1 M KOH solution at a scan rate of 5 mV s^{-1}. (c) Corresponding K-L plots. (d) Comparison of LSV for CrP/C and commercial 20% Pt/C, inset graph shows the corresponding Tafel plots. (e) Chronoamperometric measurements of CrP/C and commercial Pt/C in 0.1 M KOH solution at 0.57 V versus RHE in O_2-saturated 0.1 M KOH solution with a rotating speed of 200 rpm. (f) Methanol tolerance evaluation of CrP/C and commercial Pt/C in O_2-saturated 0.1 M KOH solution. At 1000 s methanol was added up to a 3 M concentration. For comparison, the same amount of H_2O was added at 2000 s. Inset graph showed enlarged data for CrP/C catalyst.

Stability was assessed by chronoamperometric analysis (**Figure 4e**). CrP/C-based electrodes exhibited much higher stabilities than Pt/C toward ORR in 0.1 M KOH, with a negligible degradation even after 60 h of continuous operation. In contrast, during the same operation time,

Pt/C electrodes lost approximately 60% of the initial current density. Methanol tolerance measurements were performed by adding methanol to the electrolyte during the choronoamperometric measurements. As shown in **Figure 4f**, the current density measured from CrP/C electrocatalysts showed very minor changes upon the addition of methanol, up to a 3 M concentration, into the electrolyte. The slight changes may be actually associated to the dilution of the KOH electrolyte when methanol was added to the solution. This was confirmed by a similar current density change upon addition of the same amount of H_2O into the solution, proving virtually no influence of methanol in the electrocatalytic ORR on CrP-based electrodes. Overall, CrP-based electrodes showed much higher stabilities than commercial Pt/ electrocatalysts and other electrocatalysts reported previously (**Table 1**).

Table 4.1. Comparison of different catalysts for ORR in alkaline solution.

Catalysts	J_l (mA cm^{-2})	E_h (V)	E_o (V)	Stability (h)	Reference
Co_2P	4.8	0.77	0.86	6.9	7
CoP	4.5	0.7	0.8	8.3	8
NiP-C	3.4	0.4	0.6	11.1	38
Co_2C/graphene	2.9	0.77	0.91	1.4	39
Ferric citrate-NH_4Cl	5.1	0.85	0.94	1.4	40
Fe_3O_4/N-doped graphene	4.5	0.67	0.78	5.6	33
MoC/N-doped carbon nanofibers	4.8	0.77	0.9	10	41
CrP/C	4.94	0.65	0.8	60	This paper

J_l: limit current density, E_h: half-potential, E_o: onset potential

First-principles calculations were carried out to elucidate the process and parameters behind the exceptional ORR catalytic performance of CrP and to determine the rate limiting step. In alkaline solution, the thermodynamically most favorable reaction pathway for the ORR process was considered to be the O+OH dissociation pathway, which can be divided into four steps:[37] i) adsorption of an O_2 molecule onto CrP surface site (O_2*); ii) reduction of O_2* with H_2O* to an O+OH group adsorbed on the CrP site (O+OH*); iii) transition from O+OH* to an adsorbed O*

atom; and iv) transition from O* to an adsorbed OH* (Figure 4.6). The optimized adsorption structures of O_2*, O+OH*, OH* and O* on CrP catalyst and their adsorption energies were shown in **Figure S2**. According to the density functional theory (DFT) calculations, O_2 strongly chemisorbs on CrP. The O_2 side-on adsorption was the most stable configuration, with very low adsorption energy, -3.01 eV (**Figure 5c**). The notable strength of the adsorption was corroborated by the large elongation of the O=O bond length ($d_{O=O}$ = 1.50 Å) relative to the gas-phase value ($d_{O=O}$ = 1.23 Å), making it easier for the O=O bond to be broken. These highly activated O_2* already pointed toward a potentially high ORR catalytic activity. From the charge difference it can be clearly seen that a large charge transfer exists between CrP and O_2, which contribute to the strong interaction between CrP and O_2 (**Figure 5d**). Besides, DFT calculations showed that on the surface of CrP, O_2+H rapidly dissociates to O+OH radicals (i.e. O-O bond breaking, see **Figure S2**, O+OH-x (x = 1, 2, 3)). Therefore, it is impossible to form H_2O_2 in a later process and the less efficient $2e^-$ pathway is blocked on the surface of CrP. **Figure 5** shows the free energy diagrams for $4e^-$ oxygen reduction process of CrP in alkaline medium. Two pathways were considered: i) O_2 dissociation (**Figure 5a**); and ii) O_2 hydrogenation (**Figure 5b**). As shown in **Figure 5**, O-O breaking processes ($O_2 \rightarrow 2O^*$ or $O_2^* + H_2O^* \rightarrow O+OH^* + OH^*$) are down-hill. On the other hand, $OH^* \rightarrow OH^-$ is the main uphill process owing to the strong adsorption of OH to CrP (~ 4 eV), which suggested that this is the ORR rate-limiting step.

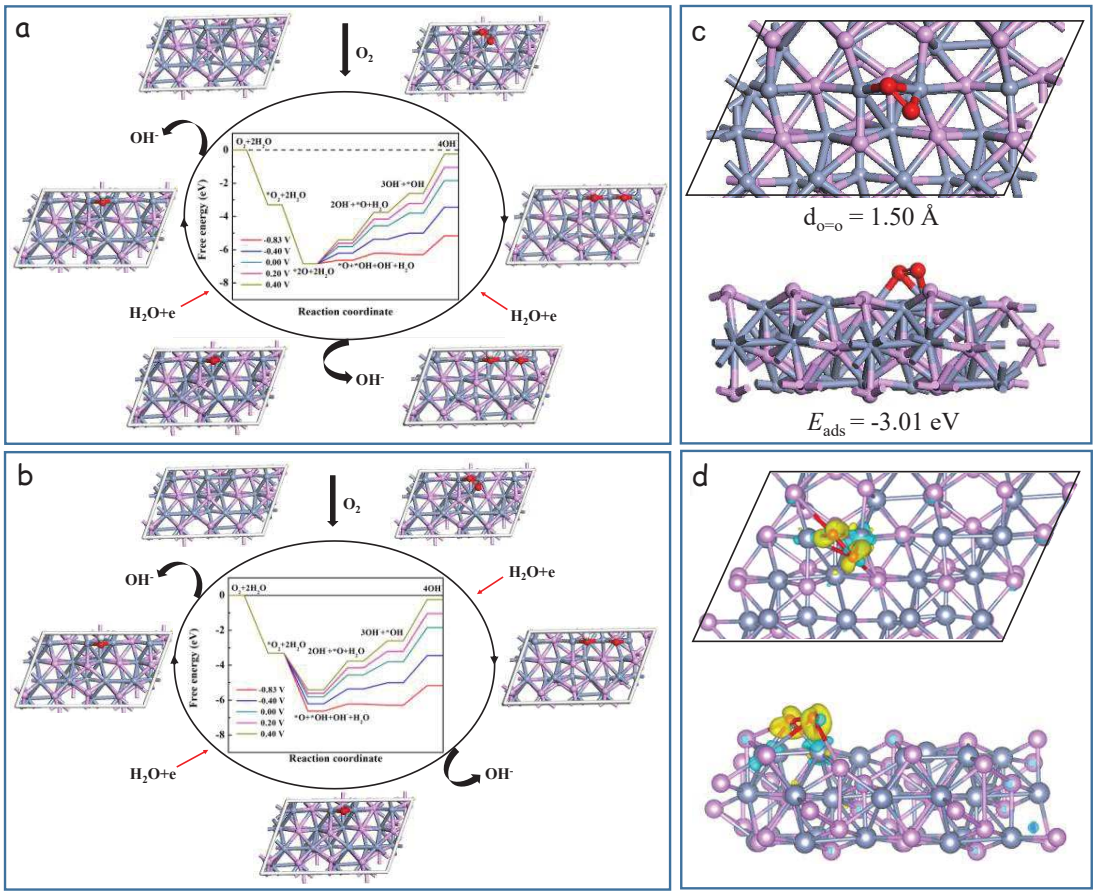

Figure 5. Free-energy diagrams for the reduction of O_2 at different electrode potential in alkaline medium on CrP for (a) O_2 dissociation pathway and (b) O_2 hydrogenation pathway. (c) The most stable structure of O_2 adsorbed on CrP. (d) The charge difference for O_2 adsorption on CrP. Isovalue = 0.005 a.u. The charge accumulation and depletion are colored in yellow and cyan.

4. Conclusions

In summary, we prepared CrP NCs via a facile one-step colloidal synthetic strategy. Compared with presented CVD methods, our solution-based strategy allows producing CrP with nanometric particle size and with a very high throughput and material yield. CrP NCs were mixed with carbon to prepare electrocatalysts for the ORR. CrP-based electrocatalysts demonstrated a high activity and stability toward ORR in an alkaline electrolyte and an absolute tolerance to methanol. DFT calculations revealed a strong adsorption of O_2 on the surface of CrP

NCs which facilitated cleavage. On the other hand, the OH^- desorption was considered the rate limiting step in the ORR reaction. Overall, CrP was demonstrated as a new low-cost and earth abundant ORR electrocatalyst with high technological potential in alkaline fuel cells and metal air batteries.

Notes

The authors declare no competing financial interest.

Acknowledgements

This work was supported by the European Regional Development Funds and the Spanish MINECO project SEHTOP (ENE2016-77798-C4- 3-R). T. Zhang and J. Arbiol acknowledge funding from Generalitat de Catalunya 2017 SGR 327 and the Spanish MINECO project ANAPHASE (ENE2017-85087-C3). ICN2 acknowledges support from the Severo Ochoa Programme (SEV-2013-0295) and is funded by the CERCA Programme / Generalitat de Catalunya. J. Llorca is a Serra Hunter Fellow and is grateful to ICREA Academia program and grants MINECO/FEDER ENE2015-63969-R and GC 2017 SGR 128. J. Liu, X. Yu, R. Du, C. Zhang and T. Zhang thank the China Scholarship Council for scholarship support. M. Meyns acknowledges a Juan de la Cierva formación grant by the Spanish MINECO. Y. Wang thanks the National Natural Science Foundation of China for financial support (Grant Nos: 21673220, 21831003, 21733004), National Key Research and Development Program of China (2016YFA0602900) and High performance Computing Center of Jilin Province and Computing Center of Jilin University for essential support. Part of the present work has been performed in the framework of Universitat Autònoma de Barcelona Materials Science PhD program.

Appendix A. Supplementary data

Supplementary material related to this article can be found, in the online version.

References

[1] P. Hernandez-Fernandez, F. Masini, D. N. McCarthy, C. E. Strebel, D. Friebel, D. Deiana, P. Malacrida, A. Nierhoff, A. Bodin, A. M. Wise, J. H. Nielsen, T. W. Hansen, A. Nilsson, I. E. L. Stephens, I. Chorkendorff, Mass-selected nanoparticles of Pt_xY as model catalysts for oxygen electroreduction, Nature Chem. 6 (2014) 732-738.

[2] Y. Wang, N. Zhao, B. Fang, H. Li, X. T. Bi, H. Wang, Carbon-Supported Pt-Based Alloy Electrocatalysts for the Oxygen Reduction Reaction in Polymer Electrolyte Membrane Fuel Cells: Particle Size, Shape, and Composition Manipulation and Their Impact to Activity, Chem. Rev. 115 (2015) 3433-3467.

[3] K. Li, R. Zhang, R. Gao, G. Shen, L. Pan, Y. Yao, K. Yu, X. Zhang, J. Zou, Metal-defected spinel $MnxCo_{3-x}O_4$ with octahedral Mn-enriched surface for highly efficient oxygen reduction reaction, Appl. Catal. B-Environ. 244 (2019) 536-545.

[4] W. Yang, X. Liu, X. Yue, J. Jia, S. Guo, Bamboo-like Carbon Nanotube/Fe_3C Nanoparticle Hybrids and Their Highly Efficient Catalysis for Oxygen Reduction, J. Am. Chem. Soc. 137 (2015) 1436-1439.

[5] S. Surendran, S. Shanmugapriya, A. Sivanantham, S. Shanmugam, R. K. Selvan, Electrospun Carbon Nanofibers Encapsulated with NiCoP: A Multifunctional Electrode for Supercapattery and Oxygen Reduction, Oxygen Evolution, and Hydrogen Evolution Reactions, Adv. Energy Mater. 8 (2018) 1800555.

[6] Q. Wang, Y. Fan, K. Wang, H. Shen, G. Li, H. Fu, Y. She, Hierarchical tubular structures composed of CoP_x and carbon nanotubes: Highly effective electrocatalyst for oxygen reduction, Carbon 130 (2018) 241-249.

[7] V. V. T. Doan-Nguyen, S. Zhang, E. B. Trigg, R. Agarwai, J. Li, D. Su, K. I. Winey, C. B. Murray, Synthesis and X-ray Characterization of Cobalt Phosphide (Co_2P) Nanorods for the Oxygen Reduction Reaction, ACS Nano 9 (2015) 8108-8115.

[8] H. Yang, Y. Zhang, F. Hu, Q. Wang, Urchin-like CoP nanocrystals as hydrogen evolution reaction and oxygen reduction reaction dual-electrocatalyst with superior stability, Nano Lett. 15 (2015) 7616-7620.

[9] A. R. J. Kucernak, K. F. Fahy, V. N. N. Sundaram, Facile synthesis of palladium phosphide electrocatalysts and their activity for the hydrogen oxidation, hydrogen evolutions, oxygen reduction and formic acid oxidation reactions, Catal. Today. 262 (2016) 48-56.

[10] H. Teller, O. Krichecski, M. Gur, A. Gedanken, A. Schechter, Ruthenium phosphide synthesis and electroactivity toward oxygen reduction in acid solutions, ACS Catal. 5 (2015) 4260-4267.

[11] J. M. Falkowski, N. M. Concannon, B. Yan, Y. Surendranath, Heazlewoodite, Ni_3S_2: A Potent Catalyst for Oxygen Reduction to Water under Benign Conditions, J. Am. Chem. Soc. 137 (2015) 7978-7981.

[12] S. Huang, Y. Meng, Y. Cao, S. He, X. Li, S. Tong, M. Wu, N-, O- and P-doped hollow carbons: Metal-free bifunctional electrocatalysts for hydrogen evolution and oxygen reduction reactions, Appl. Catal. B-Environ. 248 (2019) 239-248.

[13] X. Liu, L. Dai, Carbon-based metal-free catalysts, Nature Rev. Mater. 1 (2016) 16064.

[14] C. S. Blackman, C. J. Carmalt, T. D. Manning, I. P. Parkin, L. Apostolico, K. C. Molloy, Low temperature deposition of crystalline chromium phosphide films using dual-source atmospheric pressure chemical vapour deposition, Appl. Surf. Sci. 233 (2004) 24-28.

[15] S. Motojima, T. Higashi, Deposition and hallow crystal growth of CrP and Cr_3P by CVD process, J. Cryst. Growth. 71 (1985) 639-647.

[16] C. E. Myers, G. A. Kisacky, J. K. Klingert, Vaporization Behavior of Chromium Phosphides The Solid Two-Phase Regions $CrPCr_{12}P_7$, $Cr_{12}P_7Cr_3P$, and Cr_3PCr, J. Electrochem. Soc. 132 (1985) 236-238.

[17] T. Nagai, M. Miyake, H. Kimura, M. Maeda, Determination of Gibbs free energy of formation of Cr_3P by double Knudsen cell mass spectrometry, J. Chem. Thermodyn. 40 (2008) 471-475.

[18] A. I. Zaitsev, N. E. Shelkova, A. D. Litvina, B. M. Mogutnov, Z. V. Dobrokhotova, Thermodynamic properties and phase equilibria in the Cr-P system, J. Phase Equilib. Diff. 19 (1998) 191-199.

[19] J. Liu, M. Meyns, T. Zhang, J. Arbiol, A. Cabot, A. Shavel, Triphenyl Phosphite as the Phosphorus Source for the Scalable and Cost-Effective Production of Transition Metal Phosphides, Chem. Mater. 30 (2018) 1799-1807.

[20] J. Liu, Z. Wang, J. David, J. Llorca, J. Li, X. Yu, A. Shavel, J. Arbiol, M. Meyns, A. Cabot, Colloidal $Ni_{2-x}Co_xP$ nanocrystals for the hydrogen evolution reaction, J. Mater. Chem. A 6 (2018) 11453-11462.

[21] G. Kresse, J. Furthmuller, Efficiency of ab-initio total energy calculations for metals and semiconductors using a plane-wave basis set, J. Comp. Mater. Sci. 6 (1996) 15–50.

[22] G. Kresse, J. Hafner, Ab initio molecular dynamics for liquid metals, J. Phys. Rev. B 47 (1993) 558–561.

[23] G. Kresse, J. Hafner, Ab initio molecular-dynamics simulation of the liquid-metal–amorphous-semiconductor transition in germanium, J. Phys. Rev. B 49 (1994) 14251–14269.

[24] G. Kresse, J. Furthmuller, Efficient iterative schemes for ab initio total-energy calculations using a plane-wave basis set, J. Phys. Rev. B 54 (1996) 11169–11186.

[25] P. E. Blochle, Projector augmented-wave method, Phys. Rev. B 50 (1994) 17953–17979.

[26] G. Kresse, D. Joubert, From ultrasoft pseudopotentials to the projector augmented-wave method, Phys. Rev. B 59 (1999) 1758–1775.

[27] J. P. Perdew, K. Burke, M. Ernzerhof, Generalized gradient approximation made simple, Phys. Rev. Lett. 77 (1996) 3865–3868.

[28] H. J. Monkhorst, J. D. Pack, Special points for Brillouin-zone integrations, Phys. Rev. B 13 (1976) 5188–5192.

[29] J. K. Nørskov, J. Rossmeisl, A. Logadottir, L. Lindqvist, J. R. Kitchin, T. Bligaard, H. Jónsson, Origin of the overpotential for oxygen reduction at a fuel-cell cathode, J. Phys. Chem. B 108 (2004) 17886-17892.

[30] L. Yu, X. Pan, X. Cao, P. Hu, X. Bao, Oxygen reduction reaction mechanism on nitrogen-doped graphene: A density functional theory study, J. Catal. 282 (2011) 183-190.

[31] B. Stypula, J. Stoch, The characterization of passive films on chromium electrodes by XPS, J. Corros. Sci. 36 (1994) 2159-2167.

[32] J. F. Moulder, W. F. Stickle, P. E. Sobol, K. D. Bomben, Handbook of X-ray photoelectron spectroscopy, Perkin-Elmer (1992) pp. 77.

[33] Z. Wu, S. Yang, Y. Sun, K. Parvez, X. Feng, K. Mullen, 3D Nitrogen-Doped Graphene Aerogel-Supported Fe_3O_4 Nanoparticles as Efficient Electrocatalysts for the Oxygen Reduction Reaction, J. Am. Chem. Soc. 134 (2012) 9082-9085.

[34] C. Wei, M. Shen, K. Ai, L. Lu, Transformation from FeS/Fe_3C nanoparticles encased S, N dual doped carbon nanotubes to nanosheets for enhanced oxygen reduction performance, Carbon 123 (2017) 135-144.

[35] Y. Chen, S. Ji, Y. Wang, J. Dong, W. Chen, R. Shen, L. Zheng, Z. Zhuang, D. Wang, Y. Li, Isolated single iron atoms anchored on N-doped porous carbon as an efficient electrocatalyst for the oxygen reduction reaction, Angew. Chem. Int. Ed. 56 (2017) 6937-6941.

[36] B. Chen, R. Li, G. Ma, X. Gou, Y. Zhu, Y. Xia, Cobalt sulfide/N, S codoped porous carbon core–shell nanocomposites as superior bifunctional electrocatalysts for oxygen reduction and evolution reactions, Nanoscale 7 (2015) 20674-20684.

[37] X. Yu, D. Wang, J. Liu, Z. Luo, R. Du, L. Liu, G. Zhang, Y. Zhang, A. Cabot, Cu_2ZnSnS_4 Nanocrystals as Highly Active and Stable Electrocatalysts for the Oxygen Reduction Reaction, J. Phys. Chem. C 120 (2016) 24265-24270.

[38] F. Razmjooei, C. Pak, J. S. Yu, Phase Diversity of Nickel Phosphides in Oxygen Reduction Catalysis, ChemElectroChem 5 (2018) 1985-1994.

[39] M. D. Meganathan, S. Mao, T. Huang, G. Sun, Reduced graphene oxide intercalated Co_2C or Co_4N nanoparticles as an efficient and durable fuel cell catalyst for oxygen reduction, J. Mater. Chem. A 5 (2017) 2972-2980.

[40] J. Zhu, D. Xu, C. Wang, W. Qian, J. Guo, F. Yan, Ferric citrate-derived N-doped hierarchical porous carbons for oxygen reduction reaction and electrochemical supercapacitors, Carbon 115 (2017) 1-10.

[41] H. Wang, C. Sun, Y. Cao, J. Zhu, Y. Chen, J. Guo, J. Zhao, Y. Sun, G. Zou, Molybdenum carbide nanoparticles embedded in nitrogen-doped porous carbon nanofibers as a dual catalyst for hydrogen evolution and oxygen reduction reactions, Carbon 114 (2017) 628-634.

***Graphical Abstract**

Graphical abstract

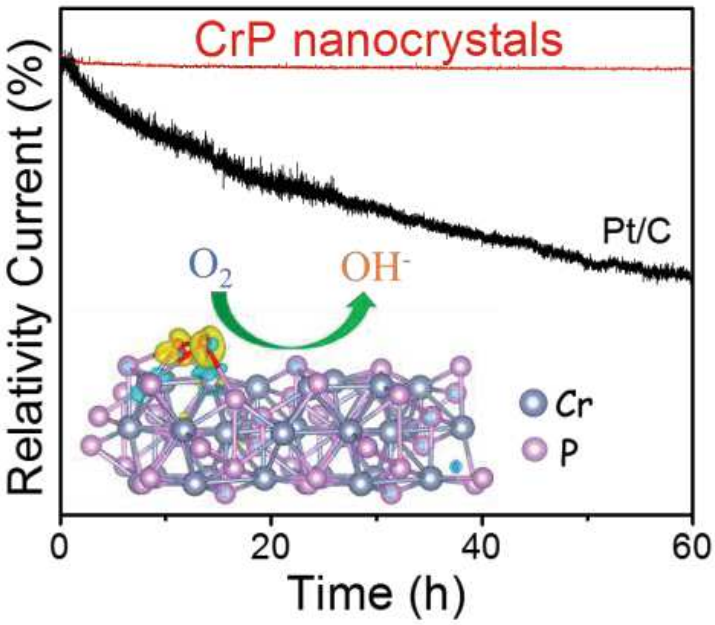

Highlights

- Chromium phosphide CrP nanocrystals were produced for the first time via a facile one-step colloidal synthetic strategy.
- CrP nanocrystals were prepared as ORR electrocatalysts for the first time.
- CrP-based electrocatalysts displayed remarkable activity and stability toward ORR and an absolute tolerance to methanol in alkaline solution.
- DFT calculations revealed CrP to provide a very strong chemisorption of O_2 that facilitates its reduction.

Supplementary Material

Click here to download Supplementary Material: JLiu_CrP_SI.pdf